



Spherical $\text{FeF}_3 \cdot 0.33\text{H}_2\text{O}$ /MWCNTs nanocomposite with mesoporous structure as cathode material of sodium ion battery

Shuangying Wei, Xianyou Wang*, Min Liu, Rui Zhang, Gang Wang, Hai Hu

National Base for International Science & Technology Cooperation, Key Laboratory of Environmentally Friendly Chemistry and Applications of Ministry of Education, Hunan Province Key Laboratory of Electrochemical Energy Storage and Conversion, School of Chemistry, Xiangtan University, Xiangtan 411105, Hunan, China

ARTICLE INFO

Article history:

Received 2 August 2017

Revised 1 October 2017

Accepted 31 October 2017

Available online 6 November 2017

Keywords:

Sodium ion batteries

Cathode material

Spherical nanoparticles

Mesoporous structure

Conductive network

ABSTRACT

$\text{FeF}_3 \cdot 0.33\text{H}_2\text{O}$ crystallizes in hexagonal tungsten bronze structure with more opened hexagonal cavities are considered as next generation electrode materials of both lithium ion battery and sodium ion battery. In this paper the mesoporous spherical $\text{FeF}_3 \cdot 0.33\text{H}_2\text{O}$ /MWCNTs nanocomposite was successfully synthesized via a one-step solvothermal approach. Galvanostatic measurement showed that the performances of sodium ion batteries (SIBs) using $\text{FeF}_3 \cdot 0.33\text{H}_2\text{O}$ /MWCNTs as cathode material were highly dependent on the morphology and size of the as-prepared materials. Benefitting from the special mesoporous structure features, $\text{FeF}_3 \cdot 0.33\text{H}_2\text{O}$ /MWCNTs nanocomposite exhibits much better electrochemical performances in terms of initial discharge capacity (350.4 mAh g^{-1}) and cycle performance (123.5 mAh g^{-1} after 50 cycles at 0.1 C range from 1.0V to 4.0V) as well as rate capacity (123.8 mAh g^{-1} after 25 cycles back to 0.1 C). The excellent electrochemical performance enhancement can be attributed to the synergistic effect of the mesoporous structure and the MWCNTs conductive network, which can effectively increase the contact area between the active materials and the electrolyte, shorten the Na^+ diffusion pathway, buffer the volume change during cycling/discharge process and improve the structure stability of the $\text{FeF}_3 \cdot 0.33\text{H}_2\text{O}$ /MWCNTs nanocomposite.

© 2017 Science Press and Dalian Institute of Chemical Physics, Chinese Academy of Sciences. Published by Elsevier B.V. and Science Press. All rights reserved.

1. Introduction

Lithium ion batteries (LIBs) have successfully captured the portable electronic markets over the past decades [1,2]. But fears of exhaustion of limited and unevenly distributed lithium resources, an alternative that can compete with LIBs technology on the global market is inevitably needed [3,4]. Sodium resources are practically inexhaustible and ubiquitous [5]. Furthermore, sodium is the second lightest and smallest alkali metal next to lithium, and has much in common with lithium in physical and chemical properties [6–8]. Given this background, intense interest in the use of sodium ion batteries (SIBs) for energy system has been rekindled [9]. Consequently, it is highly estimable to develop high performance cathode materials with potentially large specific capacity and high rate capability to store and deliver energy for SIBs [10,11].

Although the structural chemistry of the sodium battery system is much more complicated in comparison to the lithium system [12–14], similar to LIBs, various metal oxides (e.g.,

NaCoO_2 [15], NaFeO_2 [16], NaVO_2 [17], $\text{Na}_{0.66}\text{Co}_{0.5}\text{Mn}_{0.5}\text{O}_2$ [18] and $\text{NaFe}_{1/2}\text{Mn}_{1/2}\text{O}_2$ [19]), polyanion compounds (e.g., NaFePO_4 [20], $\text{Na}_3\text{V}_2(\text{PO}_4)_3$ [21] and $\text{Na}_2\text{FePO}_4\text{F}$ [22]) and metal fluorides (CoF_2 [23], MnF_2 [24] and FeF_3 [25]) based on conversion or insertion reactions all have been extensively studied as the cathode materials for SIBs. Especially, iron fluoride has attracted great interests as a prospective new class of cathode materials, which exhibit high theoretical capacity (712 mAh g^{-1} for 3 e^- transfer), low cost, abundant sources, low toxicity, and high safety. Among numerous polymorphs of iron fluorides, such as FeF_3 , $\text{FeF}_3 \cdot 0.33\text{H}_2\text{O}$, $\text{FeF}_{2.5} \cdot 0.5\text{H}_2\text{O}$, $\text{FeF}_3 \cdot 0.5\text{H}_2\text{O}$ and $\text{FeF}_3 \cdot 3\text{H}_2\text{O}$, $\text{FeF}_3 \cdot 0.33\text{H}_2\text{O}$ is of the most attention due to its unique tunnel structure which is greatly beneficial to the Na^+ storage performance [26–29]. Unfortunately, the high electro-negativity of fluorine induces a large band gap, and thus leading to a poor electronic conductivity, a very low actual capacity and fast capacity fading [30].

To overcome the above obstacles, significant efforts have currently been made; the most typical one is the preparation of carbon-metal-fluoride nanocomposites (CMFNCs) as electrode materials. Hybridizing with a conductive additive phase (such as SWNTs, 3DOM, CNHs, rGO and OMC) has been regarded as a promising strategy to enhance the electrochemical performances of

* Corresponding author.

E-mail address: xywang@xtu.edu.cn (X. Wang).

FeF₃ electrode materials, which can provide a facile electron pathway [31–33]. The decrease in particle size from bulk to nanoscale is another alternative approach to shorten ion/electrode transport distance and enlarge surface area, which facilitate conversion reaction kinetics and improve the electrochemical properties of the iron fluoride [31,34]. In our previous works, the mixed conducting matrix, such as FeF₃·xH₂O/G [35], Fe₂F₅·H₂O/G [36] and Fe₂F₅·H₂O/rGO [37], all have successfully been prepared as cathode materials for SIBs and obtained some significant results. However, the capacity and cyclic stability of FeF₃·0.33H₂O/C nanocomposite are still required to be improved. The substitution of metal elements such as Co [38] and Ti [39] for iron or N [40] and –OH [41] for fluorine element has also been considered an effective strategy to improve the intrinsic electronic conductivity and structural stability of FeF₃ cathode materials. However, some ion-doped may reduce discharge capacity and influence cyclic life. Moreover, it is difficult to control the ion doping site and may cause undesirable cation mixing [42].

Recently, the electrode materials comprising nanosize and mesoporous structure have received the researchers' extensive concern, which regard as an effective way in enhancing the electrochemical properties of FeF₃ cathode materials [43,44]. It has been previously reported that solvothermal technique is an effective approach to synthesize nanoparticle/composite with controllable morphology and size [45–47]. It is generally known that the nanosized primary particles can improve the rate capability of electrode materials due to their higher surface areas and shorter sodium ions diffusion pathway [48,49]. Additionally, the abundant mesoporous framework can increase contact area between the active material and the electrolyte as well as accommodate better the strains related to the structural transformation upon repeated charge–discharge processes [50].

Owing to its high electrical conductivities, extraordinary mechanical properties and remarkable thermal properties, multi-walled carbon nanotubes (MWCNTs) have become an ideal substrate for growing and anchoring insulating materials for energy storage applications [51–53]. Particularly, MWCNTs hold three dimensional electron conductive networks with high surface area, which facilitates the fast penetration of electrolytes and diffusion of sodium ions [54,55]. For example, Shadike et al. prepared CoS₂/MWCNT nanocomposite via a simple hydrothermal method, and it obtained a high capacity of 568 mAh g⁻¹ at 100 mA g⁻¹ after 100 cycles [56]. Wang et al. synthesized SnO₂@MWCNT nanocomposite by a solvothermal approach, and it maintained discharge capacity of 474.0 mAh g⁻¹ at 66.7 mA g⁻¹ after 50 cycles [57]. Apparently, the introduction of MWCNTs can effectively increase the specific capacity, enhance the rate capability and improve cycle performance of oxide nanomaterials as SIBs anode materials [58,59]. However, to the best of our knowledge, there is rare report for the FeF₃·0.33H₂O nanoparticles in-situ growth with MWCNTs so far.

Herein, we deliberately designed and synthesized a new spherical FeF₃·0.33H₂O/MWCNTs nanocomposite with mesoporous structure via a one-step solvothermal approach. The mesoporous nanoparticles with spherical morphology possess more stable structure and higher specific surface area compared to conventional FeF₃·0.33H₂O cathode material, and thus showing excellent electrochemical performances. In addition, the MWCNTs network can not only contribute to the electric transmission, but also promote in-situ growth for spherical FeF₃·0.33H₂O nanoparticles [60].

2. Experimental

2.1. Synthesis of FeF₃·0.33H₂O/MWCNTs nanocomposite

The FeF₃·0.33H₂O/MWCNTs nanocomposite was synthesized using MWCNTs which were preferentially treated with H₂SO₄ and

KMnO₄, hydrogen fluoride (HF) as a fluorine source, and iron(III) nitrate nonahydrate (Fe(NO₃)₃·9H₂O) as an iron source. In the typical synthesis of a composite material, 120 mg of MWCNTs (about 10 wt% to FeF₃·0.33H₂O) was added to 50 mL isopropyl alcohol solution containing 1.0 mL HF in a 100 mL Teflon beakers. The Teflon beaker was sealed with Parafilm and placed in ultrasonic water for 1 h to ensure good dispersion of the MWCNTs and create defects for FeF₃·0.33H₂O nucleation sites. 2.02 g of Fe(NO₃)₃·9H₂O was dissolved in solvent under magnetic stirring. After stirring for 20 min, the solution was heated at 150 °C for 12 h in a sealed condition, followed by cooling at the room temperature to obtain off-white precipitates. The precipitates were washed by ethanol, followed by drying under vacuum at 80 °C for 12 h. The bare material was produced following the same procedure without the addition of MWCNTs.

2.2. Characterizations of structure and morphology

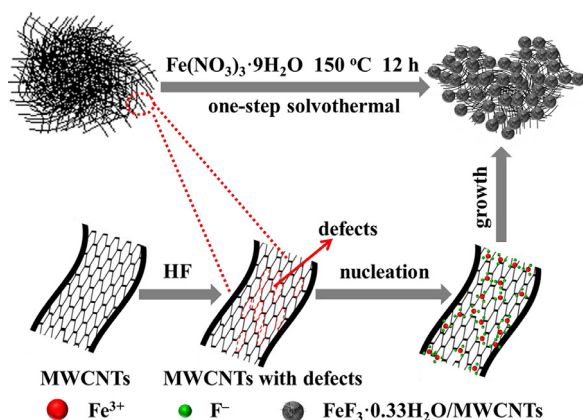
The structure and phase purity of the FeF₃·0.33H₂O and FeF₃·0.33H₂O/MWCNTs samples were characterized by using a Rigaku D/Max-3C X-ray diffractometer (XRD) with Cu K α radiation ($\lambda = 1.542 \text{ \AA}$) and a graphite monochromator operated at 40 mA and 40 kV at a scan rate of 4 °min⁻¹ from 10° to 80° (2 θ). The FTIR measurement of the samples was characterized via a Fourier transform infrared (FTIR) spectrometer (Perkin-Elmer Spectrum One) and the resolution of the apparatus is 0.09 cm⁻¹. The morphology and structure of the samples were examined by scanning electron microscope (SEM, JEOL JSM-6610LV) and transmission electron microscopy (TEM, JEOL JEM-2100F). The specific surface area of the materials was determined by Brunauer–Emmett–Teller (BET) method (TriStar II 3020, Micromeritics USA) with nitrogen as adsorption/desorption gas. The pore size distribution was determined from the adsorption branch of the isotherms by the Barrett–Joyner–Halenda (BJH) method.

2.3. Electrochemical measurements

Positive electrodes were fabricated by mixing the active material, polyvinylidene fluoride (PVDF) binder and acetylene black in *N*-methyl-2-pyrrolidone (NMP) with a weight ratio of 80:10:10. The as-prepared electrodes were cut into circular electrodes with a diameter of 10 mm and dried at 110 °C in vacuum oven for 12 h before to apply. The FeF₃·0.33H₂O and FeF₃·0.33H₂O/MWCNTs nanocomposite were used as a cathode material, metallic sodium anode and glass fiber (GF/D) from Whatman were employed as the separator, and the electrolyte was 1 mol L⁻¹ NaClO₄ in a solvent of propylene carbonate (PC). Finally, the cells were assembled in an argon-filled glove box with water and oxygen concentrations below 1 ppm. The charge/discharge cycle tests of SIBs were performed at different current densities on the Neware battery test system (Shenzhen, China) in a voltage range of 1.0–4.0 V (vs. Na⁺/Na). All electrochemical measurements were performed at room temperature.

3. Results and discussion

Scheme 1 illustrated schematically the overall procedure for the synthesis of the FeF₃·0.33H₂O/MWCNTs nanocomposite. To induce nucleation center of FeF₃·0.33H₂O on the MWCNTs surfaces, MWCNTs were firstly sonicated in HF solution to create the defects for nucleation sites. These nucleation sites could increase the affinity of MWCNTs to Fe³⁺ via electrostatic force, thus providing more growing spots for FeF₃·3H₂O nanocrystals [61]. As we known, the versatile isopropyl alcohol possesses unique physical and chemical properties such as green, low specific Hansen solubility and low boiling point, therefore, the isopropyl alcohol was introduced



Scheme 1. Schematics of fabrications of the $\text{FeF}_3 \cdot 0.33\text{H}_2\text{O}/\text{MWCNTs}$ nanocomposite.

to control the morphology and size of the final products [62–64]. In this work, we propose a simple mechanism on the synthesis process. With the introduction of the isopropyl alcohol, the nanocrystals are formed through the reaction between Fe^{3+} cations and F^- anions during the first stage of reaction. Subsequently, iron fluoride nanocrystals aggregated into nanoparticles with spherical-like morphology. As the reaction process continued, the primary nanoparticles are close to each other and self-assemble to mesoporous materials with an inside-out way [27]. In aqueous-based solution, $\text{FeF}_3 \cdot 3\text{H}_2\text{O}$ readily converted to $\text{FeF}_3 \cdot 0.33\text{H}_2\text{O}$ during one-step solvothermal treatment [24]. Moreover, these $\text{FeF}_3 \cdot 0.33\text{H}_2\text{O}$ nanocrystals were well-crystallized and can be wrapped by the fluffy MWCNTs network.

The XRD patterns of all as-obtained samples are shown in Fig. 1(a). It can be seen that a small steamed broad peak at 20° – 30° , which should be attributed to the MWCNTs [65]. All samples show intensive peaks at $2\theta = 13.8^\circ$, 23.6° and 27.8° , which are in accord with (1 1 0), (0 0 2) and (2 2 0) diffraction peaks of $\text{FeF}_3 \cdot 0.33\text{H}_2\text{O}$ (orthorhombic structure with Cmc m space group, JCPDS No. 76-1262). In the hexagonal-tungsten-bronze (HTB) $\text{FeF}_3 \cdot 0.33\text{H}_2\text{O}$ (Fig. 1(b)) structure, six Fe octahedrals are connected via corner-sharing to form a special huge hexagonal cavity. Besides, the trace amount of water can be used as a structural stabilizer, to stabilize the huge hexagonal cavity and avoid structure collapse during Na^+ insertion and extraction processes [60]. Therefore, HTB- $\text{FeF}_3 \cdot 0.33\text{H}_2\text{O}$ can provide the favorable space for accommodation and transportation of Na^+ .

The Raman spectra of pure MWCNTs and the $\text{FeF}_3 \cdot 0.33\text{H}_2\text{O}/\text{MWCNTs}$ nanocomposite were performed in Fig. 2(a). The two major bands around 1343 and 1580 cm^{-1}

are attributed to a disorder-induced phonon mode (D band) and the in-plane sp^2 vibration (G band), respectively. A shoulder band locating at 1612 cm^{-1} is observed, which can be assigned to the D' band [66]. Obviously, the $I_{\text{D}}/I_{\text{G}}$ value of the $\text{FeF}_3 \cdot 0.33\text{H}_2\text{O}/\text{MWCNTs}$ (1.80) is bigger than that of MWCNTs (1.62). The increased $I_{\text{D}}/I_{\text{G}}$ value indicates that the $\text{FeF}_3 \cdot 0.33\text{H}_2\text{O}$ nanoparticles lead to the increased disorder of MWCNTs [67]. The FT-IR spectra (Fig. 2(b)) of MWCNTs, $\text{FeF}_3 \cdot 0.33\text{H}_2\text{O}$ and $\text{FeF}_3 \cdot 0.33\text{H}_2\text{O}/\text{MWCNTs}$ were performed to confirm that the surface of $\text{FeF}_3 \cdot 0.33\text{H}_2\text{O}$ nanoparticles was decorated by the MWCNTs. The peak at 1620 cm^{-1} belongs to the vibration of H–O–H in the crystal water of $\text{FeF}_3 \cdot 0.33\text{H}_2\text{O}$. The characteristic peak at approximately 530 cm^{-1} is attributed to the typical bending vibration of Fe–F bond in $\text{FeF}_3 \cdot 0.33\text{H}_2\text{O}$. There is a peak at 1111 cm^{-1} in the spectrum of $\text{FeF}_3 \cdot 0.33\text{H}_2\text{O}/\text{MWCNTs}$, which can be attributed to the stretching vibration of C–F bond [68]. These results verify that the $\text{FeF}_3 \cdot 0.33\text{H}_2\text{O}$ nanoparticles have been successfully decorated by the MWCNTs.

The morphologies of the as-prepared samples are characterized by SEM. As seen in Fig. 3(a), the MWCNTs are wrapped around each other which form a network structure. As shown in Fig. 3(b), the $\text{FeF}_3 \cdot 0.33\text{H}_2\text{O}$ particles exhibit homogeneous spherical morphology with a uniform size of 800 nm. Besides, it can be found that the $\text{FeF}_3 \cdot 0.33\text{H}_2\text{O}$ particles are composed of interconnected nanosized primary particles with some large voids or cracks. The $\text{FeF}_3 \cdot 0.33\text{H}_2\text{O}/\text{MWCNTs}$ nanocomposite (Fig. 3(c)) maintains the original spherical morphology and the particles size reduce to 600 nm on average. Therefore, it is confirmed that MWCNTs network can limit the growth and prevent the agglomeration of $\text{FeF}_3 \cdot 0.33\text{H}_2\text{O}$ nanocrystals during the process of crystallization [69]. To accurately investigate the microstructure of the $\text{FeF}_3 \cdot 0.33\text{H}_2\text{O}$ sample, TEM image is shown in Fig. 3(d). It can be seen that the $\text{FeF}_3 \cdot 0.33\text{H}_2\text{O}$ particles were consisted of many interconnected nanosized particles with highly porous structure. As seen in Fig. 3(e), the fluffy MWCNTs network wrapped on the surface of nanoparticles, and the presence of MWCNTs could be advantageous to transfer the electrons and ions to reduce the polarization [36]. In addition, the distance of the lattice fringe with interplanar distance of 0.32 nm can be observed from the HRTEM image in Fig. 3(f), which is a typical value for (2 2 0) plane of $\text{FeF}_3 \cdot 0.33\text{H}_2\text{O}$. And it further demonstrates that the MWCNTs has entered the interior of particles rather than simply coated on the surface of particles. The incorporation of MWCNTs nanowires can significantly improve the electrical conductivity of $\text{FeF}_3 \cdot 0.33\text{H}_2\text{O}$. Meanwhile, the nanowires can also provide a three-dimensional channel for sodium ions to accelerate the transportation. It is anticipated to improve the electrochemical performance of the $\text{FeF}_3 \cdot 0.33\text{H}_2\text{O}$ cathode materials with the surface network of MWCNTs.

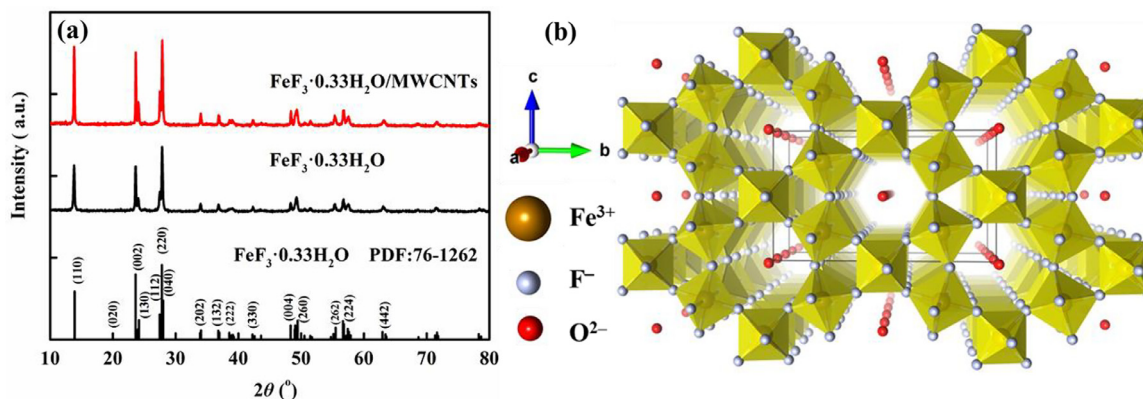


Fig. 1. (a) Powder XRD pattern of the $\text{FeF}_3 \cdot 0.33\text{H}_2\text{O}$ and $\text{FeF}_3 \cdot 0.33\text{H}_2\text{O}/\text{MWCNTs}$ cathode materials; (b) Crystallographic structure of HTB- $\text{FeF}_3 \cdot 0.33\text{H}_2\text{O}$.

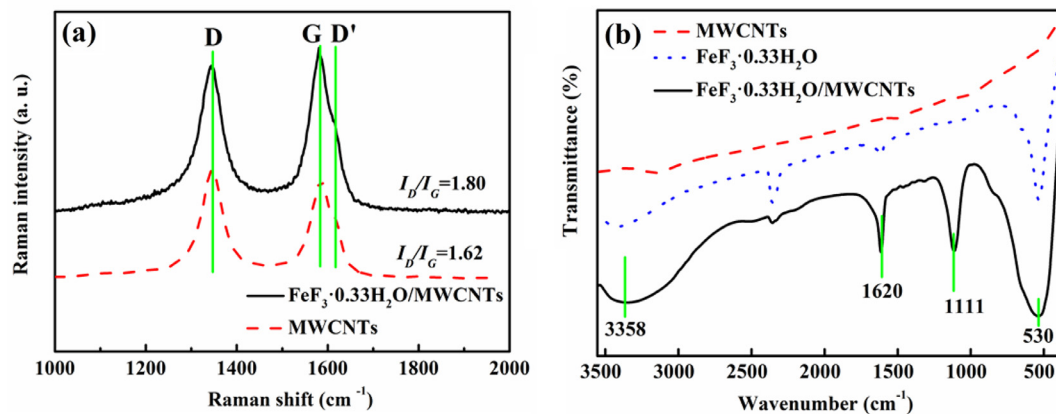


Fig. 2. (a) Raman spectra of the MWCNTs and $\text{FeF}_3 \cdot 0.33\text{H}_2\text{O}/\text{MWCNTs}$; (b) FT-IR spectra of MWCNTs, $\text{FeF}_3 \cdot 0.33\text{H}_2\text{O}$ and $\text{FeF}_3 \cdot 0.33\text{H}_2\text{O}/\text{MWCNTs}$ samples.

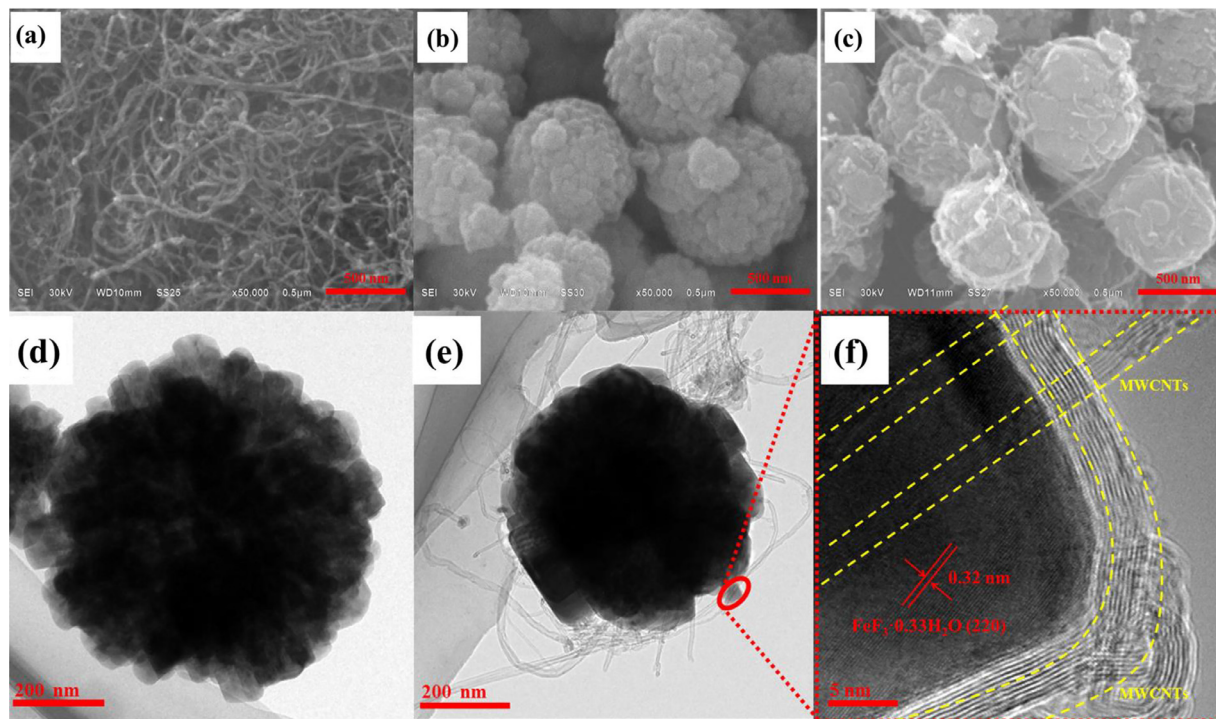


Fig. 3. SEM image of (a) MWCNTs, (b) spherical $\text{FeF}_3 \cdot 0.33\text{H}_2\text{O}$ nanoparticles, (c) $\text{FeF}_3 \cdot 0.33\text{H}_2\text{O}/\text{MWCNTs}$ nanocomposite, TEM image of (d) $\text{FeF}_3 \cdot 0.33\text{H}_2\text{O}$ nanoparticles, (e) $\text{FeF}_3 \cdot 0.33\text{H}_2\text{O}/\text{MWCNTs}$ nanocomposite, (f) HRTEM image of $\text{FeF}_3 \cdot 0.33\text{H}_2\text{O}/\text{MWCNTs}$ nanocomposite.

Table 1. Textural properties of the $\text{FeF}_3 \cdot 0.33\text{H}_2\text{O}$ and the $\text{FeF}_3 \cdot 0.33\text{H}_2\text{O}/\text{MWCNTs}$.

Samples	BET surface area ($\text{m}^2 \text{g}^{-1}$)	BJH pore volume ($\text{cm}^3 \text{g}^{-1}$)	Pore size (nm)
$\text{FeF}_3 \cdot 0.33\text{H}_2\text{O}$	33	0.067	8.4
$\text{FeF}_3 \cdot 0.33\text{H}_2\text{O}/\text{MWCNTs}$	45	0.18	14.9

The specific textural properties and porosities of the $\text{FeF}_3 \cdot 0.33\text{H}_2\text{O}$ and $\text{FeF}_3 \cdot 0.33\text{H}_2\text{O}/\text{MWCNTs}$ samples are verified by nitrogen adsorption/desorption isotherms and the corresponding BJH pore size distribution curves. According to the IUPAC classification and featured capillary condensation in the mesoporous, it can be found that the $\text{FeF}_3 \cdot 0.33\text{H}_2\text{O}$ and $\text{FeF}_3 \cdot 0.33\text{H}_2\text{O}/\text{MWCNTs}$ samples (Fig. 4(a)) appear a typical IV-type curves. As indicated in Table 1, the $\text{FeF}_3 \cdot 0.33\text{H}_2\text{O}/\text{MWCNTs}$ nanocomposite has higher surface area ($44.93 \text{ m}^2 \text{g}^{-1}$), pore volume ($0.18 \text{ cm}^3 \text{g}^{-1}$) and bigger pore size (14.84 nm) than the $\text{FeF}_3 \cdot 0.33\text{H}_2\text{O}$ nanoparticles. The higher surface area of the $\text{FeF}_3 \cdot 0.33\text{H}_2\text{O}/\text{MWCNTs}$ nanocom-

posite is beneficial to a reversible conversion reaction, because it can provide more reaction sites for charge-transfer reactions and a high electrode/electrolyte contact area [62]. Accordingly, the unique mesoporous structure allows electrolyte to penetrate easily into the inner–outer surface, which results in a shorter transport path for Na^+ , thus enhancing the cycling performance [70,71].

The cycle performance of the $\text{FeF}_3 \cdot 0.33\text{H}_2\text{O}$ and $\text{FeF}_3 \cdot 0.33\text{H}_2\text{O}/\text{MWCNTs}$ cells at 0.1 C ($1 \text{ C} = 237 \text{ mA g}^{-1}$) in the $1.0\text{--}4.0 \text{ V}$ region (vs. Na^+/Na) for 50 cycles are shown in Fig. 5(a–c). From the charge/discharge profiles of the $\text{FeF}_3 \cdot 0.33\text{H}_2\text{O}$ and $\text{FeF}_3 \cdot 0.33\text{H}_2\text{O}/\text{MWCNTs}$ cells, it can be clearly seen that both of the discharge capacities gradually decline in the first 10 cycles, and a relatively stable capacity can be maintained during the subsequent cycles. The $\text{FeF}_3 \cdot 0.33\text{H}_2\text{O}/\text{MWCNTs}$ cell can maintain a discharge capacity of 123.5 mAh g^{-1} after 50 cycles. By contrast, the $\text{FeF}_3 \cdot 0.33\text{H}_2\text{O}$ cell suffers a fast capacity fading and only delivers 82.8 mAh g^{-1} at the same rate after 50 cycles. As shown in Fig 5(c), the initial discharge capacity of $\text{FeF}_3 \cdot 0.33\text{H}_2\text{O}/\text{MWCNTs}$ cell is as high as 350.4 mAh g^{-1} , and the corresponding reversible

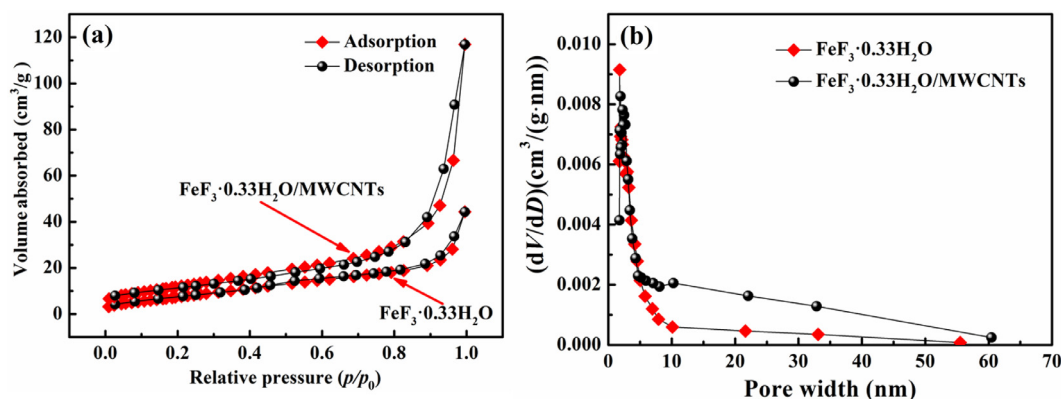
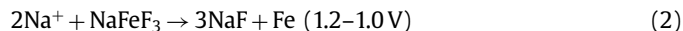
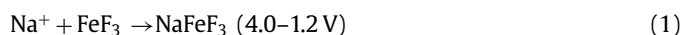


Fig. 4. (a) N_2 adsorption/desorption isotherms of the $FeF_3 \cdot 0.33H_2O$ and the $FeF_3 \cdot 0.33H_2O/MWCNTs$; (b) The BJH pore size distribution of the $FeF_3 \cdot 0.33H_2O$ and the $FeF_3 \cdot 0.33H_2O/MWCNTs$.

discharge capacity is 294.4 mAh g^{-1} . The $FeF_3 \cdot 0.33H_2O/MWCNTs$ cell can deliver a discharge capacity of 246.0 mAh g^{-1} after 5th cycle, the capacity approximately is 211.6 mAh g^{-1} at the 10th cycle and maintains 163.8 mAh g^{-1} after 30 cycles. Even so, the discharge specific capacity of the nanocomposite is superior to those of the recently reported results [35,60]. For example, Li et al. prepared $FeF_3 \cdot 0.33H_2O/SWNT$ composite via an ionothermal synthesis route and obtained a discharge capacity of 74 mAh g^{-1} at 0.1 C after 50 cycles [60]. Han et al. prepared $K_{0.6}FeF_3$ -C nanocomposites, and it delivers a low discharge capacity of 100 mAh g^{-1} at 0.1 C after 35 cycles at different cut-off voltages [72]. Shen et al. synthesized $FeF_3 \cdot xH_2O/G$ nanocomposite by a sol-gel method, and it only maintained a low discharge capacity of 101.0 mAh g^{-1} at 0.1 C after 30 cycles [35]. Apparently, the spherical $FeF_3 \cdot 0.33H_2O/MWCNTs$ nanocomposite in this work has much better excellent electrochemical performances. The $FeF_3 \cdot 0.33H_2O$ and $FeF_3 \cdot 0.33H_2O/MWCNTs$ cells were cycled at a rate of 1 C , as shown in Fig. 5(d). The first discharge capacity retentions of $FeF_3 \cdot 0.33H_2O$ and $FeF_3 \cdot 0.33H_2O/MWCNTs$ cells are about 77.7 , 112.0 mAh g^{-1} , respectively. The discharge capacity reaches 72.9 mAh g^{-1} at the 50th cycle and still maintains at 56.9 mAh g^{-1} after 100 cycles for the $FeF_3 \cdot 0.33H_2O/MWCNTs$ cell.

Rate capability is also an important parameter to evaluate electrochemical performance. As illustrated in Fig. 5(e)–(g), the rate capabilities of the $FeF_3 \cdot 0.33H_2O$ and $FeF_3 \cdot 0.33H_2O/MWCNTs$ cells are examined at 0.1 C , 0.2 C , 0.3 C , 0.5 C and 1 C rates for 5 cycles, respectively. The corresponding charge/discharge curves at varying rates are shown in Fig. 5(e) and (f). The average discharge capacity of $FeF_3 \cdot 0.33H_2O/MWCNTs$ is 241.6 mAh g^{-1} at 0.1 C . And the subsequent average discharge capacities are 134.3 mAh g^{-1} , 110.5 mAh g^{-1} and 85.3 mAh g^{-1} at 0.2 C , 0.3 C and 0.5 C , respectively. Apparently, with the increase of the C-rate, $FeF_3 \cdot 0.33H_2O/MWCNTs$ gives much higher discharge capacity and much better rate capability than $FeF_3 \cdot 0.33H_2O$. Moreover, the $FeF_3 \cdot 0.33H_2O/MWCNTs$ cell can deliver a discharge capacity of 75.0 mAh g^{-1} at 1 C . When the rate backs to 0.1 C after 25 cycles, the $FeF_3 \cdot 0.33H_2O/MWCNTs$ cell maintains a discharge capacity of 123.8 mAh g^{-1} . The enhanced electrochemical performance of $FeF_3 \cdot 0.33H_2O/MWCNTs$ cell is probably due to the large increase of the electronic conductivity after introduction of MWCNTs, which can enhance the diffusion coefficient of Na^+ and lower the activation barrier of Na^+ diffusion with the increasing rate [27,48]. Long period of constant voltage has been displayed in all 1st discharge curves for $FeF_3 \cdot 0.33H_2O/MWCNTs$ nanocomposite, and it can be ascribed to the following reasons.



Firstly, the low electrochemical activity of NaF is electronic insulative and poor compatibility with the electrolyte, which can influence the reversibility of Eq. (2) [73]. Secondly, the dynamic nature of conversion reaction and the presence of metallic nanodomains may catalyze the decomposition of the electrolyte during the first discharge process [74]. In addition, the serious solid-electrolyte-interface (SEI) layer caused by the undesirable reaction between electrode material and electrolyte during the initial discharge process may lead to this electrochemical phenomena [75,76].

The specific electrochemical feature has been displayed in all initial discharge curves for $FeF_3 \cdot 0.33H_2O/MWCNTs$ nanocomposite at $1.2\text{--}1.0 \text{ V}$. In general, the electrode reaction process of FeF_3 can be expressed to the insertion/deinsertion reaction and the reversible conversion reaction, respectively. In the first region (Eq. (1)), Na^+ is inserted into the FeF_3 framework first to form $NaFeF_3$ [75]. This process appears to be fully reversible, and the structure of pristine FeF_3 can be maintained during the Na^+ insertion process [75]. While for the second region (Eq. (2)), it involves a complete structural reconstruction due to reconversion reaction. Similar to the conversion-type anode materials (e.g., Fe_3O_4 [77], Co_3O_4 [78] and CoO [79]), the pristine structure of $NaFeF_3$ is destroyed to form NaF-Fe nanocomposites. Generally, NaF is electronic insulative and poor compatibility with the electrolyte, which can influence the reversibility of Eq. (2) [75].

Fig. 6 compares the morphology changes of the $FeF_3 \cdot 0.33H_2O$ and $FeF_3 \cdot 0.33H_2O/MWCNTs$ samples after 50 charge/discharge cycles at 0.1 C . As shown in Fig. 6(a), it presents apparent agglomeration and the structure has been distinctly damaged. On the contrary, it can be seen in Fig. 6(b) that the spherical texture of the $FeF_3 \cdot 0.33H_2O/MWCNTs$ cell is preserved essentially after long-term cycling. The essential preservation of morphology and structure further manifests that the addition of MWCNTs can significantly improve the structural stability of the $FeF_3 \cdot 0.33H_2O$ nanoparticles during long-term charge/discharge process.

Fig. 7(a) and (b) displays the GITT curves of the SIBs using $FeF_3 \cdot 0.33H_2O$ and $FeF_3 \cdot 0.33H_2O/MWCNTs$ as cathode active material during the second cycle as a function of time in the potential range of $1.0\text{--}4.0 \text{ V}$. To obtain the steady state cell voltage, the cells were firstly charged-discharged at 0.05 C for activation. Then the cells were charged at a constant current (0.1 C) for an interval τ of 10 min followed by an open-circuit voltage (OCV) for 60 min to allow the cell potential to relax to the steady-state value, E_s . The dE/dx and $dE/dt^{1/2}$ as a function of stoichiometry x in the charge process are shown in Fig. 7(c) and (d), and then the D_{Na^+} values of

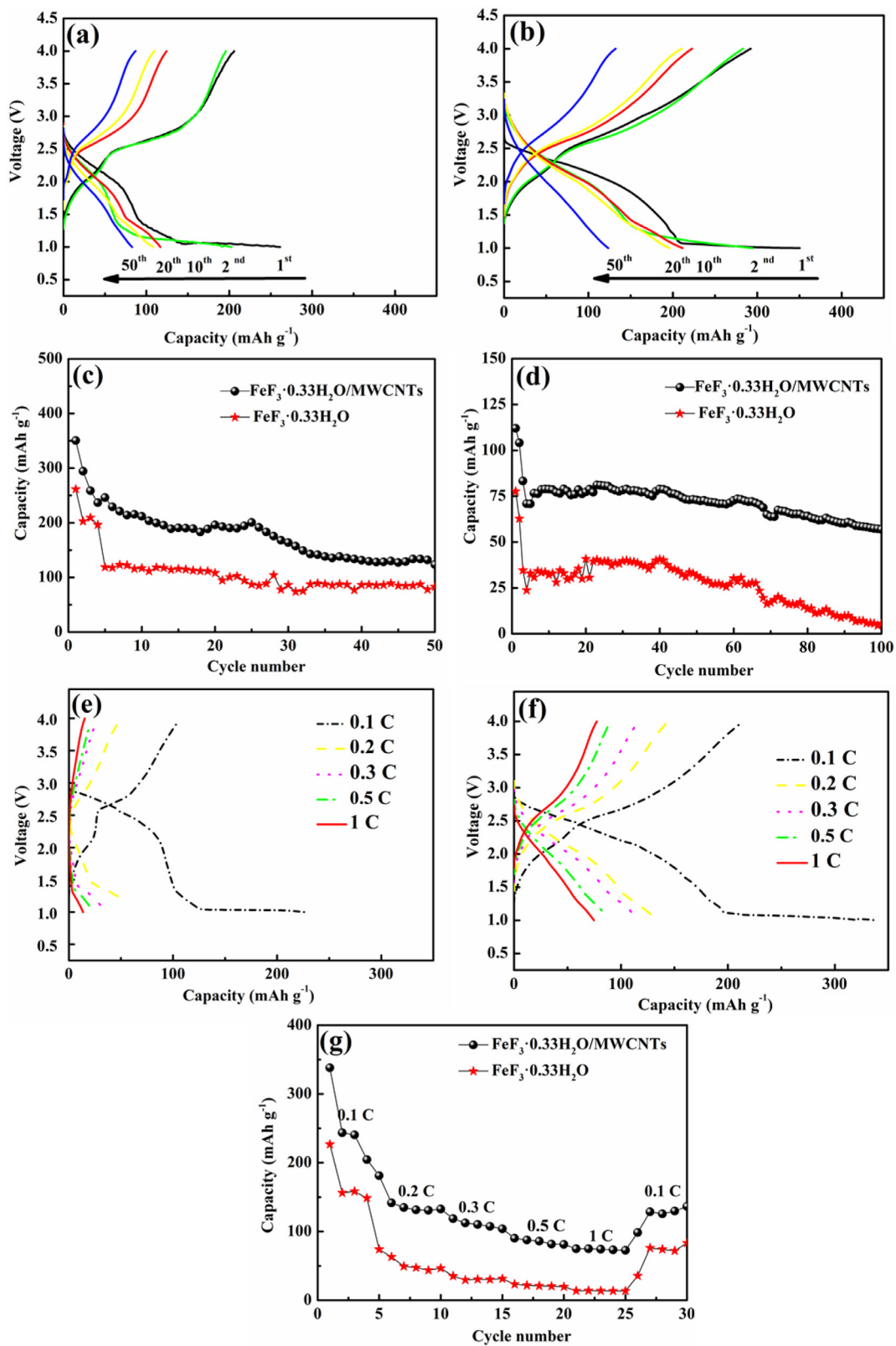


Fig. 5. Discharge and charge profiles of the (a) $\text{FeF}_3 \cdot 0.33\text{H}_2\text{O}$ and (b) $\text{FeF}_3 \cdot 0.33\text{H}_2\text{O}/\text{MWCNTs}$ cells at particular cycles (1st, 2nd, 10th, 20th, 50th); (c) Discharge capacity vs. cycle number for $\text{FeF}_3 \cdot 0.33\text{H}_2\text{O}$ and $\text{FeF}_3 \cdot 0.33\text{H}_2\text{O}/\text{MWCNTs}$ cells at 0.1 C; (d) Long term cycling performance at 1 C; The discharge/charge curves of the (e) $\text{FeF}_3 \cdot 0.33\text{H}_2\text{O}$ and (f) $\text{FeF}_3 \cdot 0.33\text{H}_2\text{O}/\text{MWCNTs}$ cells at different cycles; (g) Rate capacity of $\text{FeF}_3 \cdot 0.33\text{H}_2\text{O}$ and $\text{FeF}_3 \cdot 0.33\text{H}_2\text{O}/\text{MWCNTs}$ cells.

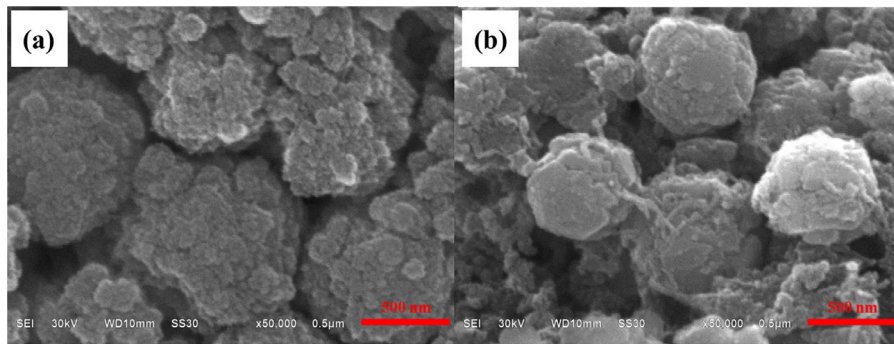


Fig. 6. SEM images of (a) $\text{FeF}_3 \cdot 0.33\text{H}_2\text{O}$ and (b) $\text{FeF}_3 \cdot 0.33\text{H}_2\text{O}/\text{MWCNTs}$ cells after 50 cycles at 0.1 C.

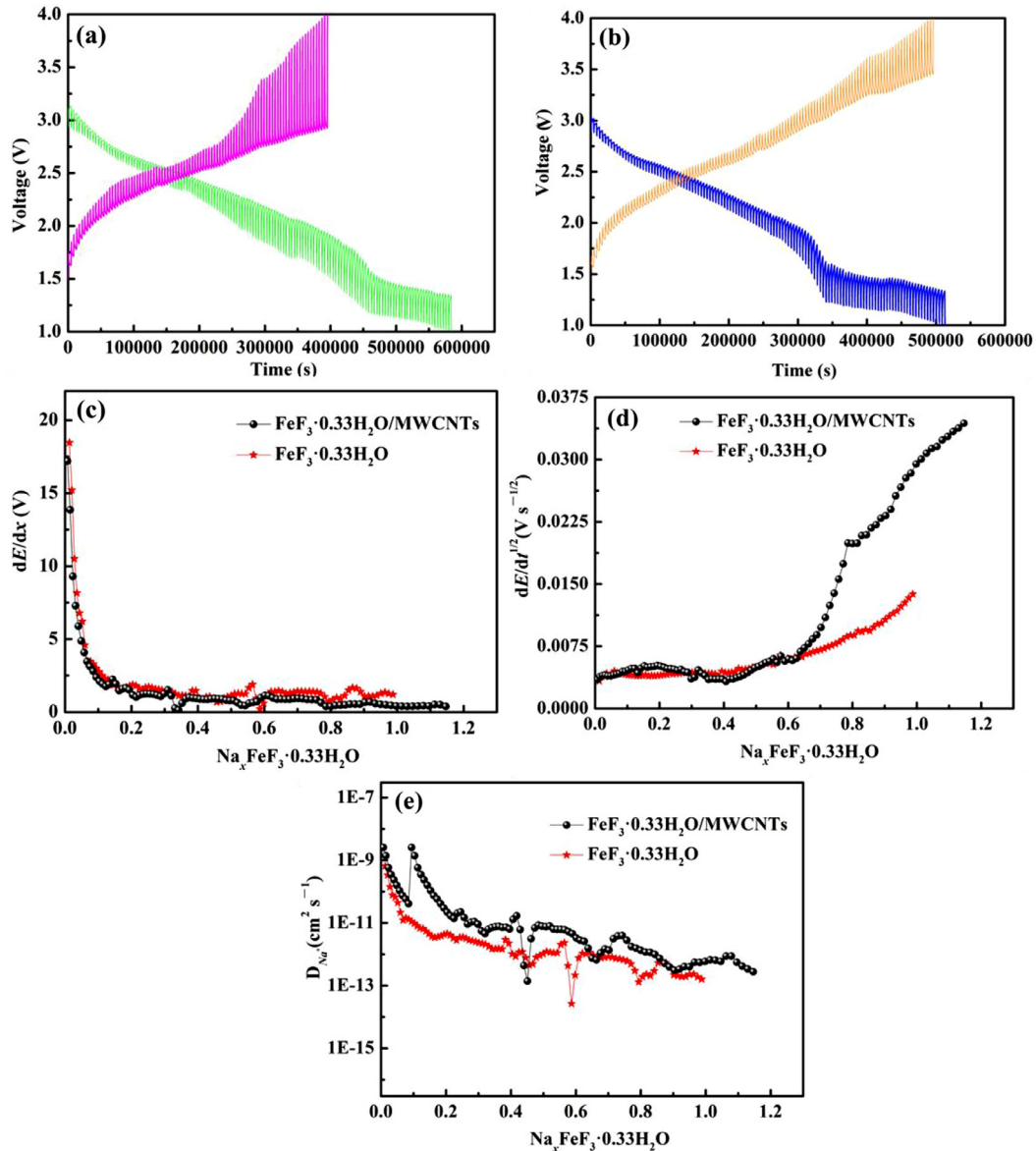


Fig. 7. The GITT curves of (a) $\text{FeF}_3 \cdot 0.33\text{H}_2\text{O}$ and (b) $\text{FeF}_3 \cdot 0.33\text{H}_2\text{O}/\text{MWCNTs}$ cells as a function of time between 1.0 V and 4.0 V; (c) dE/dx , (d) $dE/dt^{1/2}$ and (e) the calculated D_{Na^+} values for the $\text{FeF}_3 \cdot 0.33\text{H}_2\text{O}$ and $\text{FeF}_3 \cdot 0.33\text{H}_2\text{O}/\text{MWCNTs}$ cells as a function of the stoichiometry x .

$\text{FeF}_3 \cdot 0.33\text{H}_2\text{O}$ and $\text{FeF}_3 \cdot 0.33\text{H}_2\text{O}/\text{MWCNTs}$ materials can be calculated according to the values of dE/dx and $dE/dt^{1/2}$ in the following equation [25]:

$$D_{\text{Na}^+} = \frac{4}{\pi} \left[I_0 \frac{V_m}{FS} \right]^2 \left[\frac{dE/dx}{dE/dt^{1/2}} \right]^2, \quad t \ll \frac{L^2}{D_{\text{Na}^+}} \quad (3)$$

As shown in Fig. 7(e), it can be found that the D_{Na^+} values of the $\text{FeF}_3 \cdot 0.33\text{H}_2\text{O}$ cathode active material are in the range of 2.7×10^{-14} to $6.5 \times 10^{-10} \text{ cm}^2 \text{ s}^{-1}$, while the D_{Na^+} values of the $\text{FeF}_3 \cdot 0.33\text{H}_2\text{O}/\text{MWCNTs}$ cathode active material are in the range of 1.4×10^{-13} to $2.6 \times 10^{-9} \text{ cm}^2 \text{ s}^{-1}$ in the process of Na^+ extraction. Apparently, the D_{Na^+} values of the $\text{FeF}_3 \cdot 0.33\text{H}_2\text{O}/\text{MWCNTs}$ are slightly higher than $\text{FeF}_3 \cdot 0.33\text{H}_2\text{O}$.

Therefore, the remarkable electrochemical performance enhancement of the $\text{FeF}_3 \cdot 0.33\text{H}_2\text{O}/\text{MWCNTs}$ cathode material could be ascribed to the unique mesoporous structure which can effectively improve the diffusion coefficient of Na^+ , leading to high rate capability. Besides, the mesoporous structures can effectively facilitate the penetration of electrolyte into the inner regions of the active materials and provide space to buffer the volume change during charge/discharge process. Moreover, the $\text{FeF}_3 \cdot 0.33\text{H}_2\text{O}/\text{MWCNTs}$ nanoparticles assembled with three dimensional electron conductive network can not only improve the structure stability, but also shorten the Na^+ diffusion pathway and increase the Na^+ reaction sites [68].

4. Conclusions

The mesoporous spherical $\text{FeF}_3 \cdot 0.33\text{H}_2\text{O}/\text{MWCNTs}$ nanocomposite has been synthesized via one-step solvothermal approach. The addition of MWCNTs can not only increase the electronic conductivity of the $\text{FeF}_3 \cdot 0.33\text{H}_2\text{O}$ active material, but also play an important role for growth of the spherical $\text{FeF}_3 \cdot 0.33\text{H}_2\text{O}$ nanoparticles. Smaller particle's size and higher sodium ion diffusion coefficient reciprocate to the $\text{FeF}_3 \cdot 0.33\text{H}_2\text{O}/\text{MWCNTs}$ nanocomposite excellent electrochemical performance. The SIBs using $\text{FeF}_3 \cdot 0.33\text{H}_2\text{O}/\text{MWCNTs}$ as cathode active material exhibit a high initial discharge capacity of 350.4 mAh g^{-1} and maintain a discharge capacity of 123.5 mAh g^{-1} after 50 cycles at 0.1 C. Moreover, the $\text{FeF}_3 \cdot 0.33\text{H}_2\text{O}/\text{MWCNTs}$ nanocomposite also shows good rate performance. A stable discharge capacity of 123.8 mAh g^{-1} can still be resumed when the rate of 1 C back to 0.1 C after 25 cycles. Therefore, the spherical $\text{FeF}_3 \cdot 0.33\text{H}_2\text{O}/\text{MWCNTs}$ nanocomposite will be a potential cathode material for SIBs.

Acknowledgments

This work is supported financially by the National Natural Science Foundation of China under project (no. 51272221), the Key Project of Strategic New Industry of Hunan Province under project (nos. 2016GK4005 and 2016GK4030).

Supplementary materials

Supplementary material associated with this article can be found, in the online version, at [doi:10.1016/j.jechem.2017.10.032](https://doi.org/10.1016/j.jechem.2017.10.032).

References

- [1] N.-S. Choi, Z. Chen, S.A. Freunberger, X. Ji, Y.-K. Sun, K. Amine, G. Yushin, L.F. Nazar, J. Cho, P.G. Bruce, *Angew. Chem. Int. Ed.* 51 (2012) 9994–10024.
- [2] J. Liu, J.-G. Zhang, Z. Yang, J.P. Lemmon, C. Imhoff, G.L. Graff, L. Li, J. Hu, C. Wang, J. Xiao, G. Xia, V.V. Viswanathan, S. Baskaran, V. Sprenkle, X. Li, Y. Shao, B. Schwenzer, *Adv. Funct. Mater.* 23 (2013) 929–946.
- [3] S.-W. Kim, D.-H. Seo, X. Ma, G. Ceder, K. Kang, *Adv. Energy Mater.* 2 (2012) 710–721.
- [4] V. Palomares, P. Serras, I. Villaluenga, K.B. Hueso, J. CarreteroGonzález, T. Rojo, *Energy Environ. Sci.* 5 (2012) 5884–5901.
- [5] B.L. Ellis, L.F. Nazar, *Solid State Mater. Sci.* 16 (4) (2012) 168–177.
- [6] Z.L. Jian, W.Z. Han, X. Lu, H.X. Yang, Y.S. Hu, J. Zhou, Z.B. Zhou, J.Q. Li, W. Chen, D.F. Chen, L.Q. Chen, *Adv. Energy Mater.* 3 (2013) 156–160.
- [7] Y. Liu, N. Zhang, C. Yu, Li. Jiao, J. Chen, *Nano Lett.* 16 (2016) 3321–3328.
- [8] Y. Liu, N. Zhang, Li. Jiao, Z. Tao, J. Chen, *Adv. Funct. Mater.* 25 (2015) 214–220.
- [9] P. Moreau, D. Guyomard, J. Gaubicher, F. Boucher, *Chem. Mater.* 22 (2010) 4126–4128.
- [10] S.P. Ong, V.L. Chevrier, G. Hautier, A. Jain, C. Moore, S. Kim, X. Ma, G. Ceder, *Energy Environ. Sci.* 4 (2011) 3680–3688.
- [11] L. Wang, Y. Lu, J. Liu, M. Xu, J. Cheng, D. Zhang, J.B. Goodenough, *Angew. Chem. Int. Ed.* 52 (2013) 1964–1967.
- [12] Y. Park, D.S. Shin, S.H. Woo, N.S. Choi, K.H. Shin, S.M. Oh, K.T. Lee, S.Y. Hong, *Adv. Mater.* 24 (2012) 3562–3567.
- [13] Y. Cao, L. Xiao, M.L. Sushko, W. Wang, B. Schwenzer, J. Xiao, Z. Nie, L.V. Saraf, Z. Yang, J. Liu, *Nano Lett.* 12 (2012) 3783–3787.
- [14] K.H. Ha, S.H. Woo, D. Mok, N.S. Choi, Y. Park, S.M. Oh, Y. Kim, J. Kim, J. Lee, L.F. Nazar, K.T. Lee, *Adv. Energy Mater.* 3 (2013) 770–776.
- [15] R. Berthelot, D. Carlier, C. Delmas, *Nat. Mater.* 10 (2011) 74–80.
- [16] N. Yabuuchi, H. Yoshida, S. Komaba, *Electrochemistry* 80 (2012) 716–719.
- [17] M. Guignard, C. Didier, J. Darriet, P. Bordet, E. Elkaim, C. Delmas, *Nat. Mater.* 12 (2013) 74–80.
- [18] X.Q. Chen, X.L. Zhou, M. Hu, J. Liang, D.H. Wu, J.P. Wei, Z. Zhou, J. Mater. Chem. A 3 (2015) 20708–20714.
- [19] N. Yabuuchi, M. Kajiyama, J. Iwatate, H. Nishikawa, S. Hitomi, R. Okuyama, R. Usui, Y. Yamada, S. Komaba, *Nat. Mater.* 11 (2012) 512–517.
- [20] Y.J. Zhu, Y.H. Xu, Y.H. Liu, C. Luo, C.S. Wang, *Nanoscale* 5 (2013) 780–787.
- [21] S.J. Lim, D.W. Han, D.H. Nam, K.S. Hong, J.Y. Eom, W.H. Ryu, H.S. Kwon, *J. Mater. Chem. A* 2 (2014) 19623–19632.
- [22] Y. Kawabe, N. Yabuuchi, M. Kajiyama, N. Fukuhara, T. Inamasu, R. Okuyama, I. Nakai, S. Komaba, *Electrochem. Commun.* 13 (2011) 1225–1228.
- [23] J.L. Tan, L. Liu, S.P. Guo, H. Hu, Z.C. Yan, Q. Zhou, Z.F. Huang, H.B. Shu, X.K. Yang, X.Y. Wang, *Electrochim. Acta* 168 (2015) 225–233.
- [24] K. Rui, Z.Y. Wen, Y. Lu, C. Shen, Jun Jin, *ACS Appl. Mater. Interfaces* 8 (2016) 1819–1826.
- [25] Y.Q. Shen, X.Y. Wang, H. Hu, M.L. Jiang, Y.S. Bai, X.K. Yang, H.B. Shu, *RSC Adv.* 5 (2015) 38277–38282.
- [26] H. Jung, H. Song, T. Kim, J.K. Lee, J. Kim, *J. Alloys Compd.* 647 (2015) 750–755.
- [27] J.L. Tan, L. Liu, H. Hu, Z.H. Yang, H.P. Guo, Q.L. Wei, X.C. Yi, Z.C. Yan, Q. Zhou, Z.H. Huang, H. Shu, X.K. Yang, X.Y. Wang, *J. Power Sources* 251 (2014) 75–84.
- [28] L.D. Carlo, D.E. Conte, E. Kemnitz, N. Pinna, *Chem. Commun.* 50 (2014) 460–462.
- [29] Y. Lu, Z.Y. Wen, J. Jin, K. Rui, X.W. Wu, *Phys. Chem. Chem. Phys.* 16 (2014) 8556–8562.
- [30] Q.X. Chu, Z.C. Xing, J.Q. Tian, X.B. Ren, A.M. Asiri, A.O. Al-Youbi, K.A. Alamry, X.P. Sun, *J. Power Sources* 236 (2013) 188–191.
- [31] D.L. Ma, Z.Y. Cao, H.G. Wang, X.L. Huang, L.M. Wang, X.B. Zhang, *Energy Environ. Sci.* 5 (2012) 8538–8542.
- [32] X. Zhao, C.M. Hayner, M.C. Kung, H.H. Kung, *Chem. Commun.* 48 (2012) 9909–9911.
- [33] L.S. Fan, B.J. Li, N.Q. Zhang, K.N. Sun, *Sci. Rep.* 5 (2015) 12154.
- [34] S.-W. Kim, D.-H. Seo, H. Gwon, J. Kim, K. Kang, *Adv. Mater.* 22 (2010) 5260–5264.
- [35] Y.Q. Shen, X.Y. Wang, H. Hu, M.L. Jiang, X.K. Yang, H.B. Shu, *J. Power Sources* 283 (2015) 204–210.
- [36] M.L. Jiang, X.Y. Wang, Y.Q. Shen, H. Hu, Y.Q. Fu, X.K. Yang, *Electrochim. Acta* 186 (2015) 7–15.
- [37] M.L. Jiang, X.Y. Wang, S.Y. Wei, Y.Q. Shen, H. Hu, *J. Alloys Compd.* 670 (2016) 362–368.
- [38] L. Liu, M. Zhou, L.H. Yi, H.P. Guo, J.L. Tan, H.B. Shu, X.K. Yang, Z.H. Yang, X.Y. Wang, *J. Mater. Chem.* 22 (2012) 17539–17550.
- [39] S.Y. Wei, X.Y. Wang, R.Z. Yu, R. Zhang, M. Liu, Z.H. Yang, H. Hu, *J. Alloys Compd.* 702 (2017) 372–380.
- [40] J. Lee, B. Kang, *Chem. Commun.* 52 (2016) 12100–12103.
- [41] Z.H. Yang, Z.J. Zhang, Y.L. Yuan, Y.Q. Huang, X.Y. Wang, X.Y. Chen, S.Y. Wei, *RSC Adv.* 6 (2016) 75766–75776.
- [42] L. Li, B.H. Song, Y.L. Chang, H. Xia, J.R. Yang, K.S. Lee, L. Lu, *J. Power Sources* 283 (2015) 162–170.
- [43] L. Zhou, D. Zhao, X.W.(David) Lou, *Angew. Chem. Int. Ed.* 124 (2012) 243–245.
- [44] Y.M. Zhang, W.X. Zhang, Z.H. Yang, H.Y. Gu, Q. Zhu, S.H. Yang, M. Li, *Angew. Chem. Int. Ed.* 127 (2015) 4004–4008.
- [45] J. Cao, L. Wang, X.M. He, M. Fang, J. Gao, J.J. Li, L.F. Deng, H. Chen, G.Y. Tian, J.L. Wang, S.S. fan, *J. Mater. Chem. A* 1 (2013) 5955–5961.
- [46] L. Wang, X.M. He, W.T. Sun, J.L. Wang, Y.D. Li, S.S. Fan, *Nano Lett.* 12 (2012) 5632–5636.
- [47] L. Wang, W.T. Sun, X.Y. Tang, X.K. Huang, X.M. He, J.J. Li, Q.W. Zhang, J. Gao, G.Y. Tian, S.S. Fan, *J. Power Sources* 244 (2013) 94–100.
- [48] J. Liu, L. Chen, M. Hou, F. Wang, R. Che, Y. Xia, *J. Mater. Chem.* 22 (2012) 25380–25387.
- [49] M.G. Kim, M. Jo, Y.S. Hong, J. Cho, *Chem. Commun.* 2 (2009) 218–220.
- [50] F.Y. Cheng, H.B. Wang, Z.Q. Zhu, Y. Wang, T.R. Zhang, Z.L. Tao, J. Chen, *Energy Environ. Sci.* 4 (2011) 3668–3675.
- [51] B.J. Landi, M.J. Ganter, C.D. Cress, R.A. DiLeo, R.P. Raffaele, *Energy Environ. Sci.* 2 (2009) 638–654.
- [52] X.F. Zhang, T.V. Sreekumar, T. Liu, S. Kumar, *J. Phys. Chem. B* 108 (2004) 16435–16440.
- [53] S. Berber, Y.-K. Kwon, D. Tomanek, *Phys. Rev. Lett.* 84 (2000) 4613–4616.
- [54] Y.H. Yin, X.T. Zhang, Y.J. Jia, Z.X. Cao, S.T. Yang, *RSC Adv.* 5 (2015) 1447–1451.
- [55] G. Gao, Q. Zhang, X.B. Cheng, P.Y. Qiu, R.J. Sun, T. Yin, D.X. Cui, *ACS Appl. Mater. Interfaces* 7 (2015) 340–350.
- [56] Z. Shadike, M.H. Cao, F. Ding, L. Sang, Z.W. Fu, *Chem. Commun.* 51 (2015) 10486–10489.
- [57] Y. Wang, D.W. Su, C.Y. Wang, G.X. Wang, *Electrochem. Commun.* 29 (2013) 8–11.
- [58] X.S. Zhou, Z.H. Dai, J.C. Bao, Y.G. Guo, *J. Mater. Chem. A* 1 (2013) 13727–13731.
- [59] D.H. Wang, R. Kou, D. Choi, Z.G. Yang, Z.M. Nie, J. Li, L.V. Saraf, D.H. Hu, J.G. Zhang, G.L. Graff, J. Liu, M.A. Pope, I.A. Aksay, *ACS Nano* 4 (2010) 1587–1595.
- [60] C.L. Li, L. Gu, J.W. Tong, J. Maier, *ACS Nano* 5 (2011) 2930–2938.
- [61] J. Liu, Y.L. Wan, W. Liu, Z.S. Ma, S.M. Ji, J.B. Wang, Y.C. Zhou, P. Hodgson, Y.C. Li, *J. Mater. Chem. A* 1 (2013) 1969–1975.
- [62] L. Mucosuo, S. Cravanzola, F. Cesano, D. Scarano, A. Zecchina, *J. Phys. Chem. C* 119 (7) (2015) 3791–3801.

- [63] F.X. Ma, H. Hu, H.B. Wu, C.Y. Xu, Z.C. Xu, L. Zhen, X.W.(David) Lou, *Adv. Mater.* 27 (2015) 4097–4101.
- [64] H. Yu, J. Yang, H.S. Fan, *CrystEngComm.* 19 (2017) 716–721.
- [65] S.Y. Wei, X.Y. Wang, R. Zhang, H. Hu, Y.Q. Shen, Liu J, *RSC Adv.* 6 (2016) 97759–97769.
- [66] L.F. Shen, X.G. Zhang, E. Uchaker, C.Z. Yuan, G.Z. Cao, *Adv. Energy Mater.* 2 (2012) 691–698.
- [67] B.J. Li, D.W. Rooney, N.Q. Zhang, K.N. Sun, *ACS Appl. Mater. Interfaces* 5 (2013) 5057–5063.
- [68] P.K. Reddy, K. Mukkanti, D.M. Rao, *Orient. J. Chem.* 29 (2013) 1015–1019.
- [69] B.J. Li, N.Q. Zhang, K.N. Sun, *Small* 10 (2014) 2039–2046.
- [70] Y. Lu, Z.Y. Wen, J. Jin, K. Rui, X.W. Wu, *Phys. Chem. Chem. Phys.* 16 (2014) 8556–8562.
- [71] G. Wang, X.Y. Wang, L.L. Yi, R.Z. Yu, M.H. Liu, X.K. Yang, *J. Mater. Chem. A* 4 (2016) 15929–15939.
- [72] Y. Han, J.L. Hu, C.L. Yin, Y. Zhang, J.J. Xie, D.G. Yin, C.L. Li, *J. Mater. Chem. A* 4 (2016) 7382–7389.
- [73] H. Li, G. Richter, J. Maier, *Adv. Mater.* 15 (2003) 736–739.
- [74] A.J. Gmitter, F. Badway, S. Rangan, R.A. Bartynski, A. Halajko, N. Pereira, G.G. Amatucci, *J. Mater. Chem.* 20 (2010) 4149–4161.
- [75] D.L. Ma, H.G. Wang, Y. Li, Xu D, S. Yuan, X.L. Huang, X.B. Zhang, Y. Zhang, *Nano Energy* 10 (2014) 295–304.
- [76] L.S. Li, F. Meng, S. Jin, *Nano Lett.* 12 (2012) 6030–6037.
- [77] H. Liu, M.Q. Jia, Q.Z. Zhu, B. Cao, R.J. Chen, Y. Wang, F. Wu, B. Xu, *ACS Appl. Mater. Interfaces* 8 (40) (2016) 26878–26885.
- [78] G. Longoni, M. Fiore, J. Kim, Y.H. Jung., D.K. Kim, C.M. Mari, R. Ruffo, *J. Power Sources* 332 (2016) 42–50.
- [79] Y.V. Kaneti, J. Zhang, Y.B. He, Z.J. Wang, S. Tanaka, M. Hossain, Z.Z. Pan, B. Xi-ang, Q.H. Yang, Y. Yamauchi, *J. Mater. Chem. A* 5 (2017) 15356–15366.